ACS OMEGA

Open Access

http://pubs.acs.org/journal/acsodf

Article

Efficient Samarium-Grafted-C_3N_4-Doped α-MoO_3 Used as a Dye Degrader and Antibacterial Agent: In Silico Molecular Docking Study

Mohsin Shabbir, Muhammad Imran,* Ali Haider, Iram Shahzadi, Wakeel Ahmad, Anwar Ul-Hamid, Walid Nabgan,* Anum Shahzadi, Ali Al-Shanini,* Murefah mana Al-Anazy, Mohamed Adam, and Muhammad Ikram*

Cite This: *ACS Omega* 2023, 8, 34805−34815

Read Online

ACCESS | Metrics & More | Article Recommendations | Supporting Information

ABSTRACT: This study was used to evaluate the catalytic activity (CA) and bactericidal activity of α-MoO_3 and Sm-g-C_3N_4-doped α-MoO_3 composites prepared through an efficient, cost-effective coprecipitation route. Their characteristic studies verify the formation of α-MoO_3 and its composites (3, 6, and 9 mL Sm-g-C_3N_4-doped α-MoO_3), which showed high crystallinity, as confirmed by X-ray diffraction (XRD) analysis. The production of superoxide and hydroxyl radicals due to charge transfer through α-MoO_3 and g-C_3N_4 eventually forms electrons in g-C_3N_4 and holes around α-MoO_3. CA against Rhodamine B (RhB) in basic medium provides maximum results compared to acidic and neutral media. The bactericidal efficacy of the (9 mL) doped sample represents a greater inhibition zone of 6.10 mm against the negative bacterial strain *Escherichia coli*. Furthermore, in silico studies showed that the generated nanorods may inhibit DNA gyrase and dihydropteroate synthase (DHPS) enzymes.

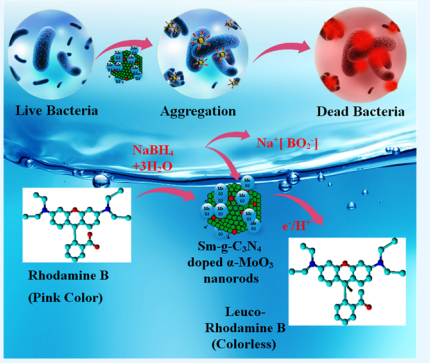

1. INTRODUCTION

Water is the preeminent necessity for every organism on land.[1] Several chemical industries have been recently considered a key source of water pollution.[2] As a significant danger to every organism, water contamination presents a formidable obstacle for society.[3] Annually, one thousand million people are affected by water pollution, and 1.8 million deaths were registered in 2015, as reported by Lancet.[4] The primary sources of water pollution are organic dyes in industrial (paper, textile, and apparel) wastewater due to their carcinogenic nature[5,6] and bacteria because of its ubiquitous nature, drug resistance, and ability to grow in the environment. Researchers estimate that between 10 and 12% of all pigments (including Rhodamine B, rose bengal, indigo red, methylene blue, and many more) are utilized yearly in the textile industry, with the majority of these colors being destroyed during their synthesis or processing. Sewage systems are becoming more contaminated by synthetic dyes that cannot be recycled, including hazardous, carcinogenic pigments. According to a World Bank report, 15−20% of water contamination is attributed to dyeing agents. In this regard, researchers have paid tremendous attention to the issue of eradicating dyes from effluents.[7] Due to the development of resistant antibiotics, infections caused by bacteria pose a significant threat to public health.[8]

Several approaches have been deployed to overcome this particular problem, including ozonation,[9] ion-exchange removal,[10] coagulation,[11] membrane filtration,[6] photocatalysis,[12] and catalytic degradation.[13] Among these methodologies, catalysis in the presence of nanomaterials is considered an inexpensive, environment-friendly, simple, and sustainable approach for treating organic dyes.[14] Several inorganic semiconductors, including Al_2O_3, ZnO, CaO, TiO_2, MgO, and MoO_3 have been utilized for catalytic dye degradation due to their distinctive features, i.e., uniform size, size distribution morphology, and a large prescribed surface area.[15] Additionally, metal oxides are extensively well known for their antimicrobial activity among the massive nanoparticles synthesized.[16]

Among the metal oxides mentioned above, molybdenum trioxide (MoO_3) has pale yellow or blue mixed-gray colored nanoparticles. MoO_3 is a semiconducting material of the n-type having a significant band gap (ranging from 2.8 to 3.2 eV) that has several possible applications,[15] including catalysis, sensors, batteries, photography, display devices, and lubricants. The MoO_3 nanomaterial, being thermally inert, can exist in three different crystalline structures of orthogonal (α-MoO_3), monoclinic (β-MoO_3), and hexagonal (h-MoO_3) MoO_3

Received: June 3, 2023
Accepted: August 29, 2023
Published: September 18, 2023

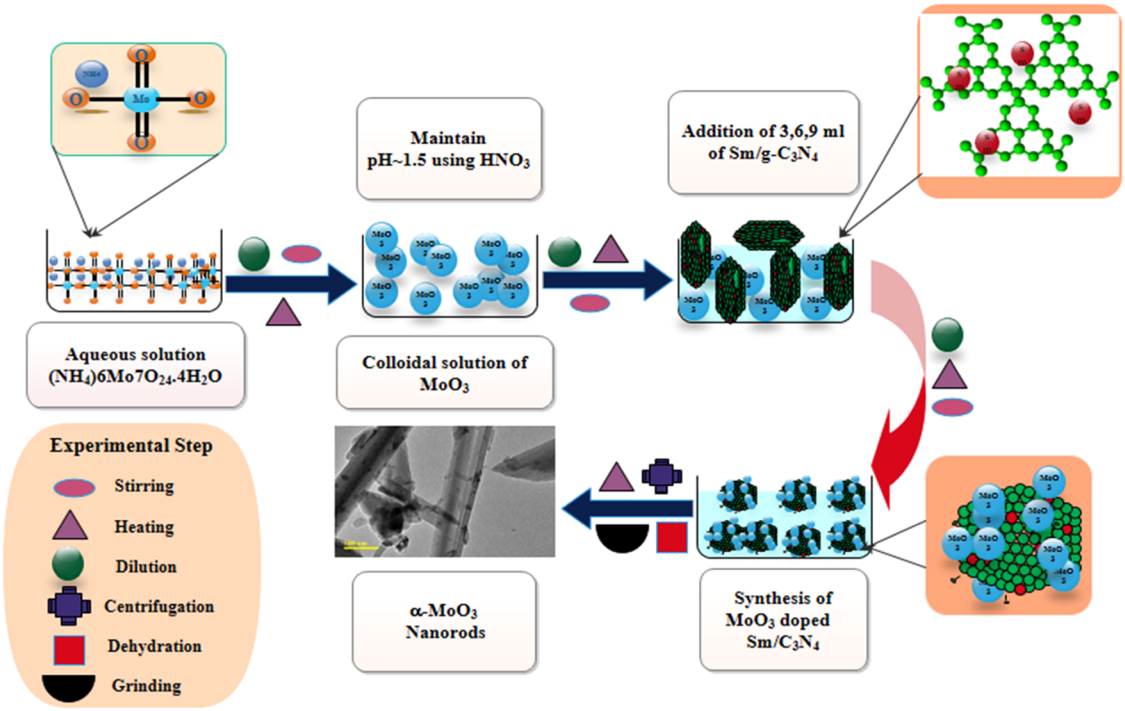

Figure 1. Schematic diagram of α-MoO_3 and Sm-g-C_3N_4-doped α-MoO_3 synthesis.

phases.[17] Several methods were used to prepare different structures and morphologies of MoO_3, such as microwave methodology, electrochemical method, sonochemical method, coprecipitation, flame synthesis, and hydrothermal process. Coprecipitation is the preferred method due to the ease in synthesizing α-MoO_3 nanomaterials and its cost-effectiveness. The physical parameters of α-MoO_3 nanoparticles must be altered to improve their performance in various nanotechnology applications. A distinctive dual layer of deformed MoO_6 octahedral atoms makes the orthorhombic crystalline structure of α-MoO_3, which is a thermodynamically stable metal oxide. MoO_3 has drawn considerable attention in biomedicine because of its low cost, nontoxicity, and biodegradability, despite its insignificantly low absorption coefficient and slow reaction kinetics limiting its further application.[18] To enhance the absorption range of MoO_3, carbon nitride in its graphitic phase (g-C_3N_4) is a metal-free semiconductor nanomaterial with a massive application in low biomedical cytotoxicity, high chemical stability, and antimicrobial activity against planktonic bacteria and viruses.[19] As reported from the literature, g-C_3N_4 has drawbacks, such as a higher recombination of charges. Various modifications were needed to enhance the catalytic activity, including metal doping and heterojunction with other semiconductors. A rare earth metal, samarium, is used in metal doping to enhance the catalytic ability of the metal oxide. Samarium (Sm), a significant rare earth (RE) ion, has drawn more attention as a result of its inexpensive cost and significant improvement in catalytic performance. The characteristics of Sm^{3+} ions include partially occupied 4f orbitals, and they are effective at capturing generated electrons, significantly slowing down the recombination of e^-/h^+ pairs.[20] Moreover, metal grafting generates nitrogen (N) defects, which act as trap sites. As reported that N-vacancies in g-C_3N_4 suppress fast recombination.[21]

This study is about the synthesis of α-MoO_3 and 3, 6, and 9 mL of Sm-g-C_3N_4-doped α-MoO_3 composites through an efficient and cost-effective coprecipitation route. Systematic characterization techniques were employed for the detailed analysis of synthesized nanocomposites. The synthesized nanocatalyst is used to eliminate the RhB dye and bacterial inactivation against *Escherichia coli*.

2. EXPERIMENTAL SECTION

2.1. Materials. Ammonium heptamolybdate tetrahydrate ($(NH_4)_6Mo_7O_{24}\cdot 4H_2O$) (AHM) and urea ($CH_4N_2O$, 99.5%) were acquired from Sigma-Aldrich. Samarium(III) nitrate hexahydrate ($Sm(NO_3)_3\cdot 6H_2O$) and HNO_3, 65% were purchased from Alfa Aesar and Merck, respectively.

2.2. Formation of Samarium-g-C_3N_4. Graphitic carbon nitride (g-C_3N_4) was synthesized by pyrolysis of urea at 550 °C over 5 h. After this, a white powder of g-C_3N_4 was achieved. Subsequently, 60 mg of g-C_3N_4 and Sm $(NO_3)_3\cdot 6H_2O$ were dispersed in 60 mL of DI water to graft in the solution form under constant stirring for 4 h. Finally, 7 mL of methanol was added to the prior solution as a sacrificial reagent.

2.3. Synthesis of α-MoO_3 and Samarium-Grafted/g-C_3N_4-Doped α-MoO_3. α-MoO_3 was prepared via coprecipitation using $(NH_4)_6Mo_7O_{24}\cdot 4H_2O$ as a precursor. Initially, 0.02 M AHM was disintegrated in 250 mL of DI water with constant agitation at around 100 °C for 1 h. A specific volume of HNO_3 was poured dropwise to maintain the pH at 1.5. Afterward, the prepared solution was centrifuged twice (at 7000 rpm) and heated at 110 °C for 12 h. The resulting MoO_3 powder was heated in a beaker at 550 °C for 3 h to obtain the final product α-MoO_3. The above route was followed to prepare Sm-g-C_3N_4 (3, 6, and 9 mL)-doped AHM, as shown in Figure 1. The reaction mechanism is proved in the equation given below (eq 1):

$$(NH_4)_6Mo_7O_{24}.4H_2O_{(aq)} + 6HNO_3 \rightarrow 7MoO_{3(S)} + 6NH_4NO_{3\,(aq)} + 7H_2O \quad (1)$$

https://doi.org/10.1021/acsomega.3c03910
ACS Omega 2023, 8, 34805−34815

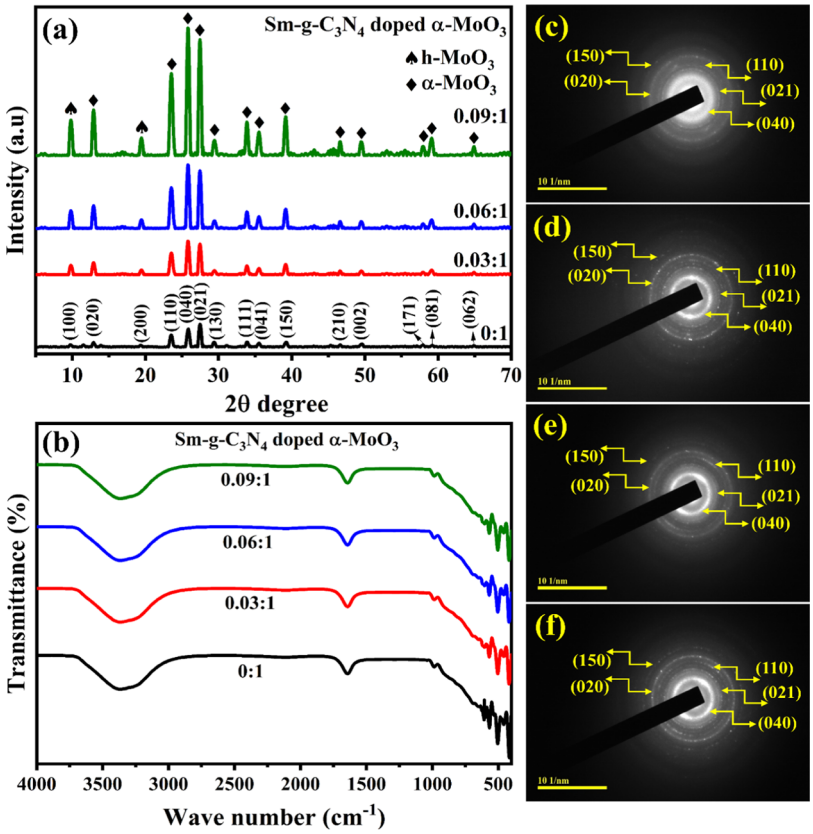

Figure 2. (a) XRD analysis of MoO_3 and Sm-g-C_3N_4-doped α-MoO_3, (b) FTIR spectra of MoO_3 and Sm-g-MoO_3, and (c–f) SAED analysis.

2.4. Catalytic Activity. The catalytic degradation of unmodified and Sm-g-C_3N_4-doped α-MoO_3 catalyst was analyzed using Rhodamine B (RhB) as a waste product. A freshly prepared sodium borohydride ($NaBH_4$) and RhB solution was used. DI water was used to dilute RhB, and a different extent of $NaBH_4$ was poured into the MoO_3 solution. The degradation efficiency can be calculated by eq 2.

$$\text{degradation rate}(\%) = \frac{C_o - C_t}{C_o} \times 100 \quad (2)$$

2.5. Isolation of *E. coli*. We cultured hospital-collected bovine mastitis milk on 5% blood agar over 24 h. The acquired colonies were strained on MacConkey agar (MA) to detect the *E. coli* (G −ve) microbe. To isolate distinct colonies of *E. coli* staining, biochemical (catalase and coagulase) techniques were performed.

2.6. Antimicrobial Activity. Antibacterial efficiency of pristine and doped MoO_3 was investigated by agar well diffusion assay to identify the effect against isolated G −ve microbes. The isolated *E. coli* microbes with 1.5 × 108 CFU mL^{-1} were wiped over a petri dish, and 6 mm diameter holes were drilled with a sterilized cork borer. When the synthesized samples were introduced into the wells at low and high concentrations (0.5 mg/50 μL and 1.0 mg/50 μL, respectively), they were compared to conventional ciprofloxacin (5 g/50 mL) and DI water (50 mL), which served as the control without the targeted sample. Formed plates were employed for antimicrobial investigation at 37 °C for 48 h. Antibacterial performance was evaluated by inhibition zone measurement using a vernier caliper.

2.7. Molecular Docking Analysis. Molecular docking on DNA gyrase and dihydropteroate synthase (PDB ID: 5MMN; (Resolution: 1.90)[22,23] and 5U0V ($DHPS_{E.\ coli}$))[24] was the focus concerning nucleic acid and folate biosynthesis pathways, separately. All three-dimensional structures were obtained through a database of proteins with the corresponding PDB IDs. Sybyl X-2.0[25] is used for docking prediction and sketch module-generated ligand complexes. After removing water atoms and adding polar H atoms, the water molecules' original energy levels were maintained in their native ligands. To visualize binding interactions in three dimensions, Pymol was employed.

2.8. Radical Scavenging Assay (DPPH). An adapted version of DPPH scavenging assay was used for evaluating antioxidant activity and free radical scavenging capacity of the synthesized NRs. A comparable amount of DPPH solution (0.1mM) was added to Sm-g-C_3N_4-doped α-MoO_3 NRs (25–150 μg/mL). This was subsequently vortexed and incubated in the dark for 30 min at ambient temperature. Ascorbic acid was used as the reference sample. The DPPH solution degradation at 517 nm was employed to determine the scavenging rate (%) of each sample, as given by eq 1.

$$\text{scavenging rate}(\%) = A_0 - A1/A_0 \times 100$$

where A_0 is the control absorbance and A_1 is the standard absorbance.

3. RESULTS AND DISCUSSION

α-MoO_3 was prepared via coprecipitation by using $(NH_4)_6Mo_7O_{24}{\cdot}4H_2O$ as a precursor.

XRD analysis is used for evaluating the crystallographic form, phase purity, and crystallinity from the synthesized α-MoO_3 and Sm-g-C_3N_4-doped α-MoO_3, as shown in Figure 2a. The XRD peaks at 12.67, 23.54, 25.81, 27.47, 29.47, 33.87,

https://doi.org/10.1021/acsomega.3c03910
ACS Omega 2023, 8, 34805−34815

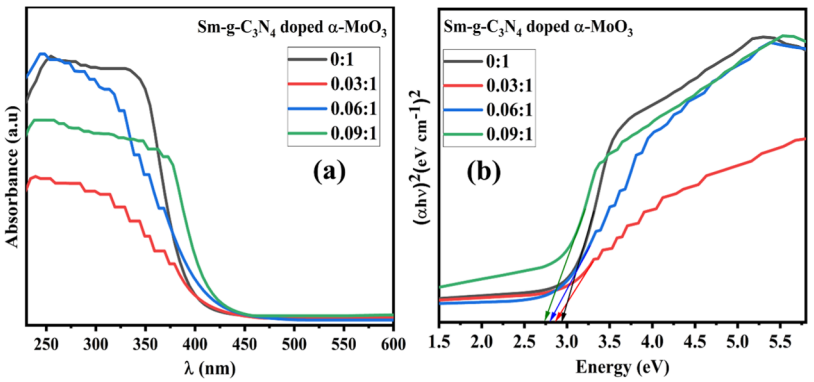

Figure 3. (a) UV−vis spectra for α-MoO_3 and Sm-g-C_3N_4-doped α-MoO_3 and (b) band gap of nanostructures.

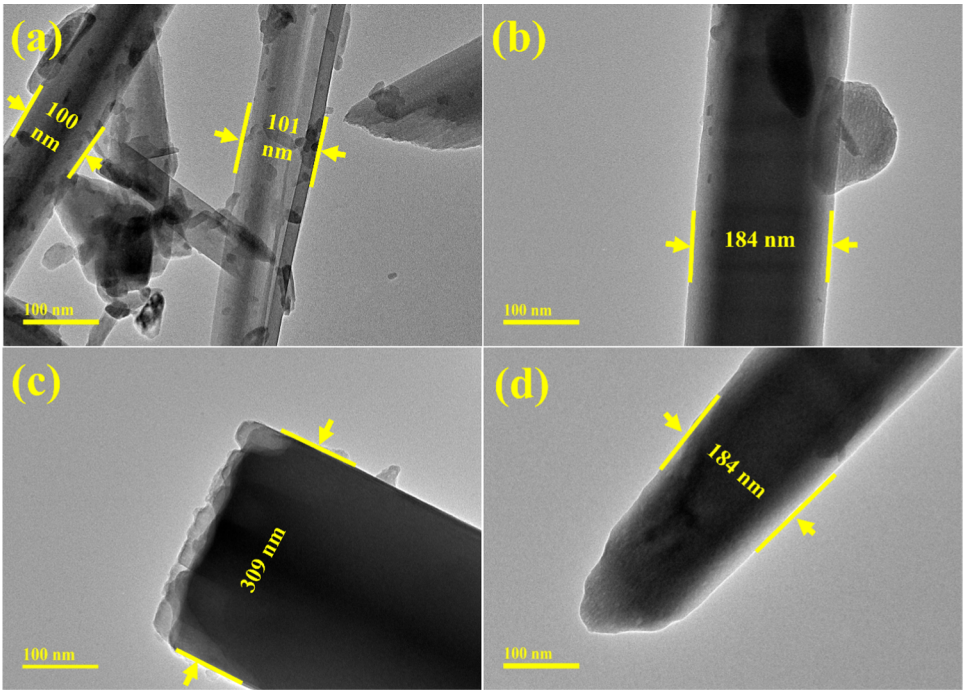

Figure 4. (a−d) TEM analysis of pure and doped α-MoO_3.

35.51, 39.16, 46.59, 49.45, 57.98, 59.11, and 64.88° assigned to the lattice planes of (020), (110), (040), (021), (130), (111), (041), (150), (210), (002), (171), (081), and (062), respectively, are exclusively indexed to orthorhombic α-MoO_3, which is well matched with JCPDS No. 05-0508. The rest of the peaks at 9.8 and 19.45° represent the diffraction planes of (100) and (200) assigned to hexagonal MoO_3 (JCPDS No. 21-0569), indicating that the phase change from hexagonal to orthorhombic is completed.[26] Furthermore, the phase stability of h-MoO_3 is at 436 °C,[27] while the resulting product is heated at 550 °C for 3 h in air, and the phase transformation occurs into orthorhombic α-MoO_3.[28] This hexagonal phase could be due to the initial low synthesis temperature and invariance under high temperatures because of the large size of nanorods. The typical (100) and (002) planes of g-C_3N_4 that emerged ∼13.12 and 27.52° seem compatible with interplanar stacking in the aromatic system and interlayer structured packing, respectively.[29] It is believed that the peaks for g-C_3N_4 in the doped system look overlaid with the peaks for α-MoO_3.[30] The crystallite size of the (040) peak of pristine and (3, 6, and 9 mL) Sm-g-C_3N_4-doped α-MoO_3, calculated using the Scherrer equation, is 36.06, 48.08, 41.21, and 41.21 nm, respectively. The interlayer spacing of the more intense peak of synthesized samples evaluated through Bragg's law ($n\lambda = 2d\sin\theta$) is 0.354−0.372 nm. Upon loading the samarium to α-MoO_3, the XRD pattern of doped nanocomposites showed the crystallinity increasing gradually. No distinctive peaks of samarium were observed in the prepared samples, which elucidates that the samarium ions are assimilated in the crystallinity of g-C_3N_4.[31]

Figure 2b shows an analysis of FTIR spectroscopy to identify functional groups within MoO_3 and doped nanorods amid the 4000 and 400 cm^{-1} range. The Mo═O bond shows stretching modes in all samples for terminal oxygen at 994 cm^{-1}.[32] A band edge of nearly 864 cm^{-1} was ascribed to the stretching vibration of Mo−O−Mo bonds.[26] The band edge found around 588 cm^{-1} exhibited stretching, whereas 484 cm^{-1} revealed the bending vibration of the Mo−O group.[33] Bands at 3550 cm^{-1} were ascribed to stretching and 1618 cm^{-1} were attributed to the bending vibrations for the hydroxyl group bonded with oxygen in water molecules, respectively.[34] The selected area electron diffraction (SAED) pattern obtained

https://doi.org/10.1021/acsomega.3c03910
ACS Omega 2023, 8, 34805−34815

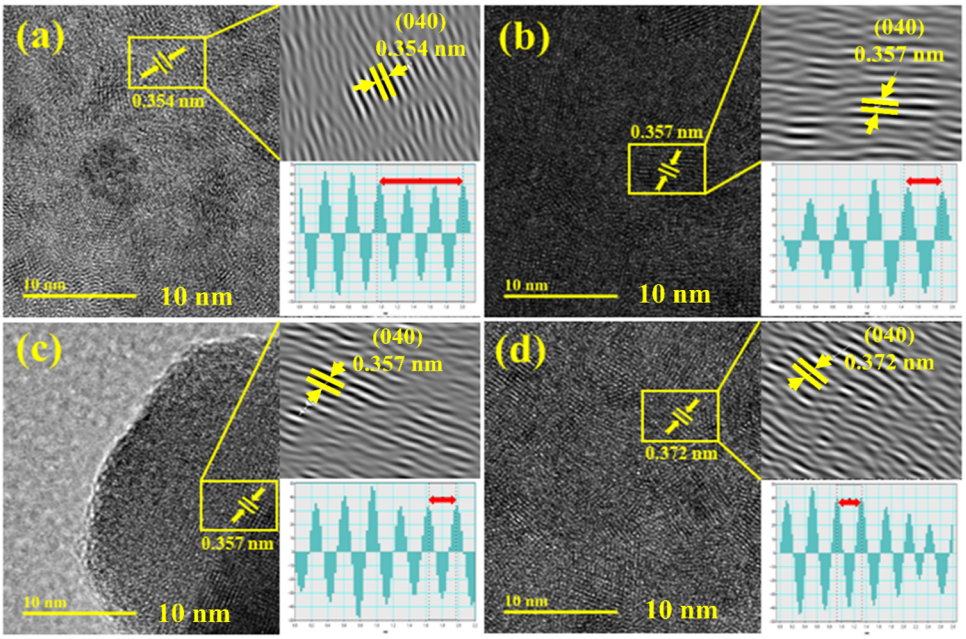

Figure 5. (a–d) Calculated *d*-spacing of α-MoO_3 and Sm-g-C_3N_4-doped α-MoO_3.

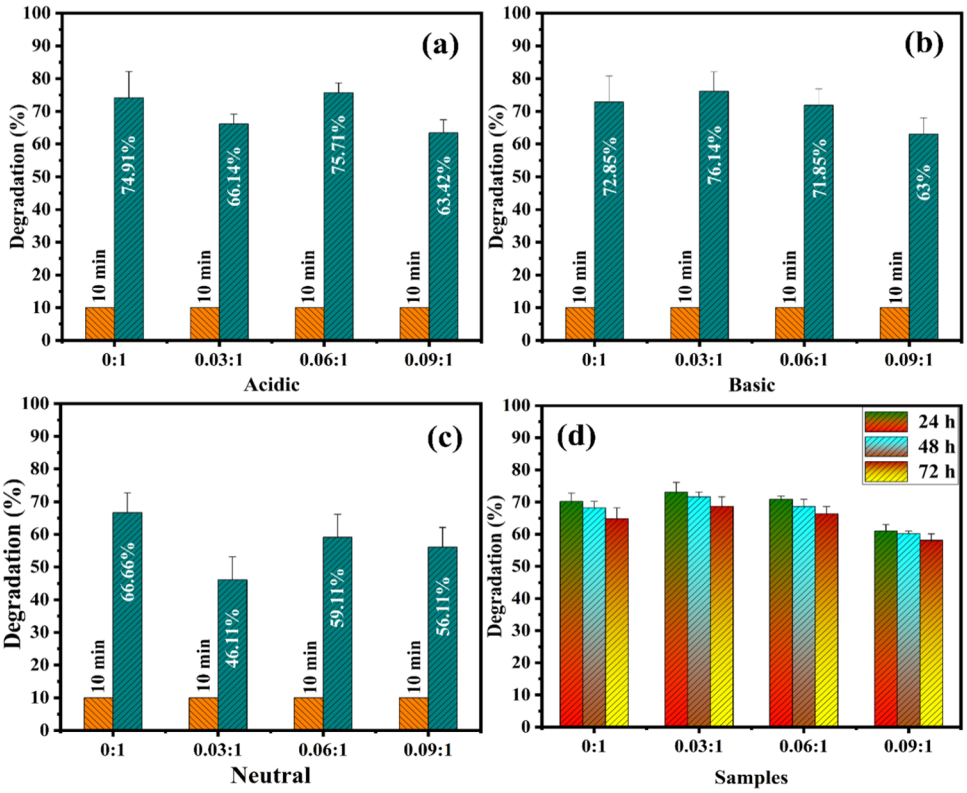

Figure 6. Catalytic activity of α-MoO_3 and (3, 6, and 9 mL) Sm-g-C_3N_4-doped α-MoO_3 in (a) acidic (b) basic, and (c) neutral environment and (d) stability of the catalyst in basic medium.

from α-MoO_3 provides information about the crystal symmetry and orientation. SAED concentric rings were indexed to correspond with the (210), (110), (040), (021), (130), and (171) crystallographic planes, which were assigned to orthorhombic α-MoO_3 following the XRD analysis, as shown in Figure 2c–f.

UV–visible spectroscopy was applied to evaluate the absorption and band gap energy of the produced α-MoO_3 in the 200–600 nm range. All samples absorbed light at a wavelength of 230–450 nm, and the maximum absorption edge was at 410, 420, and 450 nm, respectively, as shown in Figure 3a. Molybdenum causes a blue shift in the composite, and higher absorption by doped α-MoO_3 aligns with the observed hue change from yellow to blue.[35] A red shift suggested that the catalyst absorbs more visible light, enhancing its catalytic activity. This proves the existence of

https://doi.org/10.1021/acsomega.3c03910
ACS Omega 2023, 8, 34805–34815

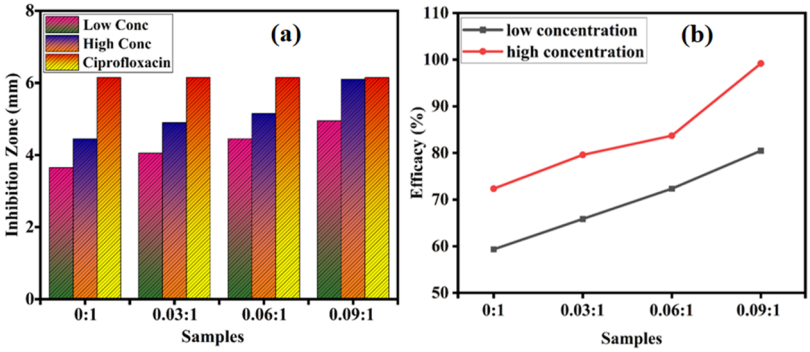

Figure 7. Antimicrobial performance of pristine and doped α-MoO_3. (a) Inhibition zone measurement (mm) and (b) % efficacy of *E. coli*.

α-MoO_3 nanorods due to the MoO_3 d−d transition.[36] The band gap energy of bare and doped composites was calculated using the Tauc plot equation of 2.94−2.75 eV, which is well agreed with the literature shown in Figure 3b.[37] The absorption wavelength exhibited a red shift for doped composites favorable to more electron−hole generation, resulting in superior catalytic efficacy and antimicrobial performance.[38]

Figure S1a−d displays the EDX spectra of the synthesized α-MoO_3 and doped α-MoO_3 nanostructures. The synthesized α-MoO_3 nanostructure in the final form confirms the presence of two elements, Mo and O, in the spectrum (Figure S1a). The Na impurity peak observed in the spectrum could be due to an operator error (Figure S1b), while coating on samples to minimize the charging effect gives rise to the Au peak in the obtained spectra. The sample holder utilized in the EDX experiment may be accountable for the Cu peaks seen in Figure S1a−d.

TEM images of pristine and doped α-MoO_3 were obtained to identify the nanorod morphology, as shown in Figure 4a−d. TEM images indicate that the surface of the doped samples is smooth compared to that of the synthesized α-MoO_3 nanorods. The diameters of synthesized nanorods calculated by ImageJ software are 100 and 101 nm (for the control sample), 184 nm (for 3 mL doped α-MoO_3), 309 nm (for 6 mL doped α-MoO_3), and 184 nm (for 9 mL doped α-MoO_3), as shown in Figure 4a−d. Variations in the size of nanorods represent the surface of α-MoO_3. The Sm-g-C_3N_4 nanocomposite had good adhesion, as shown in Figure 4a,b. Upon loading of Sm-g-C_3N_4, agglomeration of nanorods may occur and form a large rod-like lamellar morphology, as shown in Figure 4c, which may cause a reduction in the surface-to-volume ratio that limits the efficacy of CA and can be seen in the catalysis discussion later. Furthermore, microporosity is the main cause limiting the effect of the nanocatalyst instead of its large surface area, which prevents the diffusing process of the reactant.[39]

The interlayer *d*-spacing of the synthesized α-MoO_3 and Sm-g-C_3N_4-doped α-MoO_3 nanocomposites were evaluated through HRTEM images using Gatan DigitalMicrograph software, as shown in Figure 5a−d. The distances between the lattice fringes of pure and 3 mL doped α-MoO_3 are 0.354 and 0.357 nm well index to the (040) plane of the pristine and doped α-MoO_3 nanocomposite, as shown in Figure 5a,b. The interlayer spacing of 6 and 9 mL of Sm-g-C_3N_4-doped α-MoO_3 around 0.357 and 0.372 nm (Figure 5c,d) synchronized well with the XRD results.

The CA analysis of bare and Sm-g-C_3N_4-doped α-MoO_3 nanorods with $NaBH_4$ for RhB diminution was evaluated using a UV−vis spectrophotometer. The experiment was performed three times and the absorption data was extracted from the spectrophotometer. Each sample showed maximal RhB degradation 46.11 ± 6−66.66 ± 6% in a neutral medium (pH ∼ 7), 63.42 ± 8−75.71 ± 4% in an acidic medium (pH ∼ 3.5), and 63 ± 8−76.14 ± 5% in a basic medium (pH ∼ 11.5), as shown in Figure 6a−c, respectively. In an aqueous solution, the RhB dye indicates a maximum absorption peak at 554 nm.[40] CA is directly affected by catalyst structure, particle dimension, and morphology.[41] No significant dye reduction was observed without the reducing agent and nanocatalyst.[42] Adsorption happened when a catalyst and a reducing agent were introduced into the RhB solution. Initially, $NaBH_4$ dissolved in water and dissociated into BH_4^-, which acts as the reductant species, and the RhB dye behaves like an acceptor when adsorbed on the catalyst surface that acts as an electronic relay, as shown in Figure S2, which is responsible for the change of RhB dye into loco RhB (LRhB).[43,44] The adsorption of RhB and BH_4^- improved substantial active sites in nanostructures, which increases the efficiency of dye reduction.

The cationic character of RhB, which improved the adsorption capacity on the material surface, is credited with the reasonable results of CA in a basic medium. Reduced RhB adsorption on a positively charged surface indicates dye reduction effectiveness in basic media. The maximum reduction for the 3 mL doped sample in the basic environment was related to the excessive activating sites on the catalyst surface. Significant effects of catalysis are shown in basic media on account of the stronger electrostatic contact amid the negatively charged catalyst and the positively charged surface RhB dye.

It is economically important to examine the stability of the nanocatalyst. As previously stated, maximum dye degradation results are produced by CA in the basic media. To examine the stability of synthesized samples in a basic environment, the degraded solution in the presence of nanocatalyst was kept in the dark for 72 h. In this scenario, the dye had been preserved in dark conditions, and the repeated degradation spectra in every 24 h were deliberated using a UV−vis spectrophotometer, as shown in Figure 6d. According to the results, under stable conditions for 72 h, no loss in degradation was evaluated that affirmed the stability of nanocatalysts.

The antimicrobial performance of pristine and doped α-MoO_3 against *E. coli* was examined in vitro via the agar well diffusion method, as shown in Figure 7a,b. According to the

https://doi.org/10.1021/acsomega.3c03910
ACS Omega 2023, 8, 34805−34815

results, the calculated inhibition zone for *E. coli* ranged from 3.65 to 4.95 mm for low doses and 4.45−6.10 mm for high doses, respectively (Table 1). Considerable % efficacy of pure

Table 1. Bactericidal Potential of Pure and (3, 6, and 9 mL) Sm-g-C_3N_4-Doped α-MoO_3 NRs

	E. coli inhibition zone (mm)	
samples	0.5 mg/50 μL	1.0 mg/50 μL
MoO_3	3.65	4.45
3 mL	4.05	4.90
6 mL	4.45	5.15
9 mL	4.95	6.10
ciprofloxacin	6.15	6.15
DIW	0	0

and doped α-MoO_3 composites was improved against *E. coli*, rising from 19 to 30.6% and 42.5 to 55.6% for small and high doses, respectively, as shown in Figure 7b. In contrast to DI water (0 mm), the −ve and +ve control ciprofloxacin had an inhibitory zone of 6.15 mm for *E. coli* pathogens. Nevertheless, α-MoO_3 is effective against the bacteria *E. coli*.[45]

The cell wall of G −ve bacteria is complicated because it comprises an inner peptidoglycan layer and an outer lipopolysaccharide layer; *E. coli* is a complex organism.[46]

Nanostructures interfere with the functions of cells by reacting with the amide, phosphate, and carboxyl moieties, and the cell wall is damaged due to interfacial interactions.[47] A nano−bio interface is crucial for a better understanding of the bactericidal activity[48,42] describing the interaction between a nanostructure and any living component or biomaterial. In our research, α-MoO_3 and (3, 6, and 9 mL) Sm-g-C_3N_4-doped α-MoO_3 nanostructures and bacterial strains interact due to their compact dimension, and considerable surface-to-volume proportions have been attributed to their ability to kill bacteria. Sm-g-C_3N_4 improved the bactericidal efficiency by enhancing a positive charge on the catalyst surface that interacts with an oppositely charged membrane, causing membrane destruction, as shown in Figure S3.[16,49] Table 2 presents a comparison of the antibacterial activity of synthesized NSs with previous research and the results of the current investigation.

Table 2. Literature Comparison of the Antibacterial Activity of Synthesized NSs with the Present Study

nanocatalyst	synthesis route	antibacterial activity (mm) (*E. coli*)	references
h-MoO_3	chemical bath deposition	0	50
MoO_3	epigallocatechin gallate-mediated approach	0.25	51
Sm-g-C_3N_4-doped α-MoO_3	coprecipitation	6.10	present work

Following that, cells may undergo apoptosis as a response to the oxidative stress process by an abundance of reactive oxygen radicals. Increased quantities of ROS like $^*O_2$, *OH, and $^*H_2O_2$ are produced throughout the chemical process. According to systematic research, oxygen vacancy has a significant impact on bactericidal activity.[52] The influence of the α-MoO_3 nanostructures enhanced the antimicrobial effect due to their ability to produce ROS. However, the overactive ROS can also result in significant oxidative stress.[8,53,54] When α-MoO_3, either in its natural state or with Sm incorporation, is exposed to light with photon energies equal to or exceeding the energy band gap, electrons undergo a transition from the valence band (VB) to the conduction band (CB), resulting in the generation of voids within the valence band. Superoxide anion radicals ($^*O_2^-$) are created when oxygen molecules capture these accelerated electrons in the CB. Hydroxyl (OH^-) and hydrogen (H^+) ions are generated due to the reaction between water molecules (H_2O) and holes (h^+) in the VB. H^+ and superoxide anion radicals ($^*O_2^-$) combine to form the hydroperoxyl radical ($^*HO_2$) that further reacts with e^- and h^+ again, and hydrogen peroxide radicals ($^*H_2O_2$) are created. Moreover, the superoxide anion radicals ($^*O_2$) and the hydrogen peroxide radical ($^*H_2O_2$) can react to form the hydroxyl ion (OH^-), the singlet oxygen ($^1O_2$), and the hydroxyl radical (*OH). All of the reaction mechanisms are illustrated in eqs 3−8.[16]

$$MoO_3 + h\nu \rightarrow h^+ + e^- + Mo^{6+} \quad (3)$$

$$e^- + O_2 \rightarrow {}^*O_2^- \quad (4)$$

$$h^+ + HO_2 \rightarrow OH^- + H^+ \quad (5)$$

$$O_2^- + H^+ \rightarrow {}^*HO_2 \quad (6)$$

$$^*HO_2 + e^- + h^+ \rightarrow {}^*H_2O_2 \quad (7)$$

$$^*H_2O_2 + {}^*O_2^- \rightarrow {}^{-*}OH + O_2 + OH^- \quad (8)$$

The microbicidal potential of metal ion-containing nanocomposites and their interaction with bacteria via electrostatic, Van der Waals, or aquaphobic forces have been the subject of extensive research.[55,56] The molecular analysis of nanorods disclosed possible potential associations toward particular enzyme active sites, as shown in Figure 8a,b. These nanorods of Sm-g-C_3N_4-doped α-MoO_3 exhibited modest DNA gyrase binding energies, demonstrating their indispensable H-bond interaction with Gly75, Thr165, Arg76, and Gly77 with binding scores of 4.81 (Figure 8a,c), indicating its potential function as a DNA gyrase inhibitor.

In $DHPS_{E.\ coli}$, the docking score was 3.71, and H-bonding with Arg255, Glu60, and Asn22 (Figure 8b,d) was observed. Enzyme activity ceases when the substrate cannot access the active site due to ligand binding. For selected targets, in silico predictions of their binding patterns in the active pocket revealed them as effective enzyme inhibitors.

Antioxidant effects of active radical species were studied using DPPH scavenging activity (Figure 9), which are interrelated with their potential to transfer hydrogen or electrons to the DPPH free radical, producing stable diamagnetic compounds.[25,53] All produced samples showed dose-dependent behavior; however, at a concentration of 150 μg/mL, (0.03:1) NRs scavenged maximum DPPH radicals (51.89%) by donating hydrogen atoms. The formation of highly reactive $^\bullet OH$ and $^\bullet O_2$ radical species that can interact with the DPPH free radicals results in its degradation, which is highly correlated with the standard (ascorbic acid). Upon further addition of Sm-g-C_3N_4, a significant drop in antioxidant activity up to 40.5% was observed at the same concentration. This decrease in antioxidant potential might be attributed to an increase in turbidity of the test sample, which in turn caused an

https://doi.org/10.1021/acsomega.3c03910
ACS Omega 2023, 8, 34805−34815

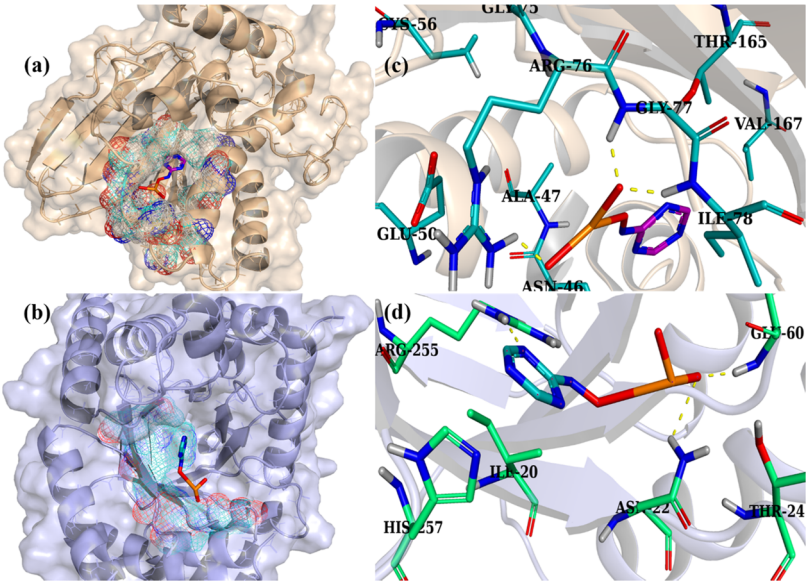

Figure 8. Native ligand binding inside the active pocket. (a, b) 3D binding interaction of Sm-g-C_3N_4-doped α-MoO_3 for (a, c) DNA $gyrase_{E.\ coli}$ and (b, d) $dihydropteroate\ synthase_{E.\ coli}$ ($DHPS_{E.\ coli}$).

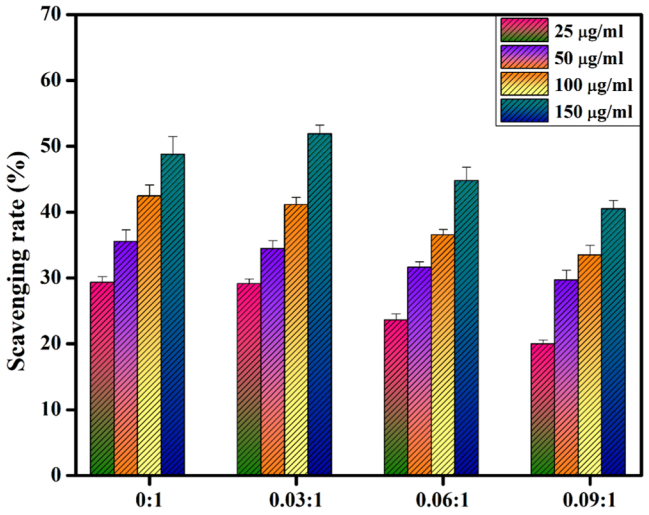

Figure 9. Scavenging potential of synthesized NRs.

antagonistic interaction, resulting in depleted scavenging activity.[1]

4. CONCLUSIONS

This study aimed to explore the catalytic capacity and bactericidal inactivation of Sm-g-C_3N_4-doped α-MoO_3 composites by an effective, low-cost coprecipitation route. XRD results confirm the phase transformation from h-MoO_3 to orthorhombic α-MoO_3, while absorption analyses of pristine and doped α-MoO_3 show a red shift and describe the decreasing trend in band gap energy from 2.94 to 2.75 eV, respectively. All constituent functional groups in the synthesized samples are confirmed by FTIR analysis and the further evaluation of elements is verified by EDX spectroscopy. TEM images provide evidence of the α-MoO_3 nanorod-like structure of all samples, and after doping, high agglomeration was observed. HRTEM images of pure and 3, 6, and 9 mL of Sm-g-C_3N_4-doped α-MoO_3 showed lattice fringes at 0.354, 0.357, 0.357, and 0.372 nm respectively, which are well matched to the (040) plane of the pristine and doped α-MoO_3 nanocomposite in XRD patterns. CA against Rhodamine B (RhB) in basic environments gives maximum results compared to acidic and neutral environments. The bactericidal efficacy of (9 mL) Sm-g-C_3N_4-doped α-MoO_3 represents a greater inhibition zone of 6.10 mm against G −ve *E. coli*. In silico assertions concurred with the microbicidal efficacy toward *E. coli* and proposed these nanorods as potential DHPS and DNA gyrase antagonists.

4.1. Challenges and Future Prospects. The low manufacturing yield of MoO_3 remains an obstacle in catalytic performance; however, these issues could be resolved by logically designing the structure and elucidating the mechanisms.

Doping produces defects in the structure of g-C_3N_4-based materials that enhanced the catalytic and antimicrobial inactivation. But excessive amounts of doping and defect may damage the structure of g-C_3N_4 and reduce the catalytic activity. It is necessary to find the optimal condition for doping and resultant defects, which increase the performance of the synthesized nanocatalyst.

However, despite our research on the absorbing and reacting characteristics of samarium, many important questions, especially how imperfections affect the surface response of samarium oxides in various oxidation states, should be studied.

■ ASSOCIATED CONTENT

Data Availability Statement

Data will be available on demand from the corresponding author.

Supporting Information

The Supporting Information is available free of charge at https://pubs.acs.org/doi/10.1021/acsomega.3c03910.

EDS, mechanism of catalysis, and antibacterial mechanism (Figures S1−S3) (PDF)

https://doi.org/10.1021/acsomega.3c03910
ACS Omega 2023, 8, 34805−34815

AUTHOR INFORMATION

Corresponding Authors

Muhammad Imran − *Department of Chemistry, Government College University, Sahiwal 57000 Punjab, Pakistan*; Email: imran@mail.ipc.ac.cn

Walid Nabgan − *Departament d'Enginyeria Química, Universitat Rovira i Virgili, 43007 Tarragona, Spain*; orcid.org/0000-0001-9901-862X; Email: walid.nabgan@urv.cat

Ali Al-Shanini − *College of Petroleum and Engineering, Hadhramout University, Mukalla 50511 Hadhramout, Yemen*; orcid.org/0000-0002-7616-7814; Email: a.alshanini@hu.edu.ye

Muhammad Ikram − *Solar Cell Applications Research Lab, Department of Physics, Government College University Lahore, Lahore 54000 Punjab, Pakistan*; orcid.org/0000-0001-7741-789X; Email: dr.muhammadikram@gcu.edu.pk

Authors

Mohsin Shabbir − *Department of Chemistry, Government College University, Sahiwal 57000 Punjab, Pakistan*

Ali Haider − *Department of Clinical Sciences, Faculty of Veterinary and Animal Sciences, Muhammad Nawaz Shareef, University of Agriculture, Multan 66000 Punjab, Pakistan*

Iram Shahzadi − *Punjab University College of Pharmacy, Allama Iqbal Campus, University of Punjab, Lahore 54000, Pakistan*

Wakeel Ahmad − *Solar Cell Applications Research Lab, Department of Physics, Government College University Lahore, Lahore 54000 Punjab, Pakistan*

Anwar Ul-Hamid − *Core Research Facilities, Research Institute, King Fahd University of Petroleum & Minerals, Dhahran 31261, Saudi Arabia*; orcid.org/0000-0002-0259-301X

Anum Shahzadi − *Faculty of Pharmacy, The University of Lahore, Lahore 54000, Pakistan*

Murefah mana Al-Anazy − *Department of Chemistry, College of Sciences, Princess Nourah bint Abdulrahman University (PNU), Riyadh 11671, Saudi Arabia*

Mohamed Adam − *Department of Radiological Sciences, College of Applied Medical Sciences, King Khalid University, Abha 61421, Saudi Arabia*

Complete contact information is available at: https://pubs.acs.org/10.1021/acsomega.3c03910

Notes

The authors declare no competing financial interest.
The manuscript is free from any conflict of interest.

ACKNOWLEDGMENTS

The research was funded by the Princess Nourah bint Abdulrahman University Researchers Supporting Project number (PNURSP2023R7), Princess Nourah bint Abdulrahman University, Riyadh, Saudi Arabia. The authors extend their appreciation to the Deanship of Scientific Research at King Khalid University, Saudi Arabia for funding this work through the Large Groups Project under the grant number L.R.G.P2/516/44.

REFERENCES

(1) Ali Ahmad, S. O.; Ikram, M.; Imran, M.; Naz, S.; Ul-Hamid, A.; Haider, A.; Shahzadi, A.; Haider, J. Novel prism shaped C_3N_4-doped Fe@Co_3O_4 nanocomposites and their dye degradation and bactericidal potential with molecular docking study. *RSC Adv.* **2021**, *11*, 23330−23344.

(2) Wang, C.-C.; Li, J.-R.; Lv, X.-L.; Zhang, Y.-Q.; Guo, G. Photocatalytic organic pollutants degradation in metal−organic frameworks. *Energy Environ. Sci.* **2014**, *7*, 2831−2867.

(3) Dias, E. M.; Petit, C. Correction: Towards the use of metal−organic frameworks for water reuse: a review of the recent advances in the field of organic pollutants removal and degradation and the next steps in the field. *J. Mater. Chem. A* **2016**, *4*, 3565.

(4) Yang, M. A Current Global View of Environmental and Occupational Cancers. *J. Environ. Sci. Health, Part C* **2011**, *29*, 223−249.

(5) Chiu, Y.-H.; Chang, T.-F.; Chen, C.-Y.; Sone, M.; Hsu, Y.-J. Mechanistic Insights into Photodegradation of Organic Dyes Using Heterostructure Photocatalysts. *Catalysts* **2019**, *9*, No. 430.

(6) Rafiq, A.; Ikram, M.; Ali, S.; Niaz, F.; Khan, M.; Khan, Q.; Maqbool, M. Photocatalytic degradation of dyes using semiconductor photocatalysts to clean industrial water pollution. *J. Ind. Eng. Chem.* **2021**, *97*, 111−128.

(7) Kant, R. Textile dyeing industry an environmental hazard. *Nat. Sci.* **2012**, *04*, No. 17027.

(8) Zhang, Y.; Li, D.; Tan, J.; Chang, Z.; Liu, X.; Ma, W.; Xu, Y. Near-Infrared Regulated Nanozymatic/Photothermal/Photodynamic Triple-Therapy for Combating Multidrug-Resistant Bacterial Infections via Oxygen-Vacancy Molybdenum Trioxide Nanodots. *Small* **2021**, *17*, No. 2005739.

(9) Naseem, K.; Farooqi, Z. H.; Begum, R.; Wu, W.; Irfan, A.; Al-Sehemi, A. G. Silver Nanoparticles Engineered Polystyrene-Poly(N-isopropylmethacrylamide-acrylic acid) Core Shell Hybrid Polymer Microgels for Catalytic Reduction of Congo Red. *Macromol. Chem. Phys.* **2018**, *219*, No. 1800211.

(10) Niu, P.; Liu, G.; Cheng, H.-M. Nitrogen Vacancy-Promoted Photocatalytic Activity of Graphitic Carbon Nitride. *J. Phys. Chem. C* **2012**, *116*, 11013−11018.

(11) Nezamzadeh-Ejhieh, A.; Karimi-Shamsabadi, M. Decolorization of a binary azo dyes mixture using CuO incorporated nanozeolite-X as a heterogeneous catalyst and solar irradiation. *Chem. Eng. J.* **2013**, *228*, 631−641.

(12) Li, Z.; Wang, G.; Zhai, K.; He, C.; Li, Q.; Guo, P. Methylene blue adsorption from aqueous solution by loofah sponge-based porous carbons. *Colloids Surf., A* **2018**, *538*, 28−35.

(13) Derikvandi, H.; Nezamzadeh-Ejhieh, A. Designing of experiments for evaluating the interactions of influencing factors on the photocatalytic activity of NiS and SnS2: Focus on coupling, supporting and nanoparticles. *J. Colloid Interface Sci.* **2017**, *490*, 628−641.

(14) Ahmad, P. T.; Jaleh, B.; Nasrollahzadeh, M.; Issaabadi, Z. Efficient reduction of waste water pollution using GO/γMnO2/Pd nanocomposite as a highly stable and recoverable catalyst. *Sep. Purif. Technol.* **2019**, *225*, 33−40.

(15) Shaheen, I.; Ahmad, K. S.; Ali, D.; Almarzouq, M. H.; Hussain, S. A.; Manohrdas, S. Bio Framework-Derived Facile MoO_3-NiO-PdO-Pd Nanomaterial for Detoxification of Organic Pollutants. *Int. J. Nanomed.* **2020**, *15*, 5591−5602.

(16) Sen, S. K.; Munshi, M. R.; Kumar, A.; Mortuza, A. A.; Manir, M. S.; Islam, M. A.; Hossain, M. N.; Hossain, M. K. Structural, optical, magnetic, and enhanced antibacterial properties of hydrothermally synthesized Sm-incorporating α-MoO_3 2D-layered nanoplates. *RSC Adv.* **2022**, *12*, 34584−34600.

(17) Pradeesh, G.; Nguyen, T. D.; Ponnuswamy, V.; Marnadu, R.; Chandrasekaran, J.; Shkir, M. Synthesis of Single-Phase MoO_3-Nanoparticles Using Various Acids for the Fabrication of n-MoO_3/p-Si Junction Diode. *J. Inorg. Organomet. Polym. Mater.* **2021**, *31*, 2638−2647.

(18) Cao, M.; Chang, Z.; Tan, J.; Wang, X.; Zhang, P.; Lin, S.; Liu, J.; Li, A. Superoxide Radical-Mediated Self-Synthesized Au/MoO_3−x Hybrids with Enhanced Peroxidase-like Activity and Photothermal Effect for Anti-MRSA Therapy. *ACS Appl. Mater. Interfaces* **2022**, *14*, 13025−13037.
(19) Chithambararaj, A.; Rajeswari Yogamalar, N.; Bose, A. C. Hydrothermally Synthesized h-MoO_3 and α-MoO_3 Nanocrystals: New Findings on Crystal-Structure-Dependent Charge Transport. *Cryst. Growth Des.* **2016**, *16*, 1984−1995.
(20) Li, G.; Wang, R.; Wang, B.; Zhang, J. Sm-doped mesoporous g-C_3N_4 as efficient catalyst for degradation of tylosin: Influencing factors and toxicity assessment. *Appl. Surf. Sci.* **2020**, *517*, No. 146212.
(21) Wang, X.; Wu, L.; Wang, Z.; Wu, H.; Zhou, X.; Ma, H.; Zhong, H.; Xing, Z.; Cai, G.; Jiang, C.; Ren, F. C/N Vacancy Co-Enhanced Visible-Light-Driven Hydrogen Evolution of g-C_3N_4 Nanosheets Through Controlled He^+ Ion Irradiation. *Solar RRL* **2019**, *3* (4), 1800298.
(22) Panchaud, P.; Bruyère, T.; Blumstein, A.-C.; Bur, D.; Chambovey, A.; Ertel, E. A.; Gude, M.; Hubschwerlen, C.; Jacob, L.; Kimmerlin, T.; et al. Discovery and Optimization of Isoquinoline Ethyl Ureas as Antibacterial Agents. *J. Med. Chem.* **2017**, *60*, 3755−3775.
(23) Ikram, M.; Rasheed, F.; Haider, A.; Naz, S.; Ul-Hamid, A.; Shahzadi, A.; Haider, J.; Shahzadi, I.; Hayat, S.; Ali, S. Photocatalytic and antibacterial activity of graphene oxide/cellulose-doped TiO_2 quantum dots: in silico molecular docking studies. *Nanoscale Adv.* **2022**, *4*, 3764−3776.
(24) Dennis, M. L.; Lee, M. D.; Harjani, J. R.; Ahmed, M.; DeBono, A. J.; Pitcher, N. P.; Wang, Z.-C.; Chhabra, S.; Barlow, N.; Rahmani, R.; et al. 8-Mercaptoguanine Derivatives as Inhibitors of Dihydropteroate Synthase. *Chem. - Eur. J.* **2018**, *24*, 1922−1930.
(25) Shahzadi, I.; Islam, M.; Saeed, H.; Haider, A.; Shahzadi, A.; Haider, J.; Ahmed, N.; Ul-Hamid, A.; Nabgan, W.; Ikram, M.; Rathore, H. A. Formation of biocompatible MgO/cellulose grafted hydrogel for efficient bactericidal and controlled release of doxorubicin. *Int. J. Biol. Macromol.* **2022**, *220*, 1277−1286.
(26) Hu, H.; Deng, C.; Xu, J.; Zhang, K.; Sun, M. Metastable h-MoO_3 and stable α-MoO_3 microstructures: controllable synthesis, growth mechanism and their enhanced photocatalytic activity. *J. Exp. Nanosci.* **2015**, *10*, 1336−1346.
(27) Bai, S.; Chen, S.; Chen, L.; Zhang, K.; Luo, R.; Li, D.; Liu, C. C. Ultrasonic synthesis of MoO_3 nanorods and their gas sensing properties. *Sens. Actuators, B* **2012**, *174*, 51−58.
(28) Wongkrua, P.; Thongtem, T.; Thongtem, S. Synthesis of h- and α-MoO_3 by Refluxing and Calcination Combination: Phase and Morphology Transformation, Photocatalysis, and Photosensitization. *J. Nanomater.* **2013**, *2013*, No. 702679.
(29) Patnaik, S.; Swain, G.; Parida, K. M. Highly efficient charge transfer through a double Z-scheme mechanism by a Cu-promoted MoO_3/g-C_3N_4 hybrid nanocomposite with superior electrochemical and photocatalytic performance. *Nanoscale* **2018**, *10*, 5950−5964.
(30) Alshammari, A. H.; Alshammari, M.; Alhassan, S.; Alshammari, K.; Alotaibi, T.; Taha, T. A. MoO_3/S@g-C_3N_4 Nanocomposite Structures: Synthesis, Characterization, and Hydrogen Catalytic Performance. *Nanomaterials* **2023**, *13*, No. 820.
(31) Sivakumar, S.; Thangadurai, T. D.; Nataraj, D. Role of Interfacial AuNPs in Solid-state Direct Z-scheme MoS_2/Au/g-C_3N_4 Heterojunction Nanocomposite's Pollutant Degradation activity under sunlight. *Colloids Surf., A* **2023**, *667*, No. 131365.
(32) Gowtham, B.; Ponnuswamy, V.; Pradeesh, G.; Chandrasekaran, J.; Aradhana, D. MoO_3 overview: hexagonal plate-like MoO_3 nanoparticles prepared by precipitation method. *J. Mater. Sci.: Mater. Electron.* **2018**, *29*, 6835−6843.
(33) Huang, L.; Zhang, F.; Li, Y.; Wang, H.; Wang, Q.; Wang, C.; Xu, H.; Li, H. Chemical reduction implanted oxygen vacancy on the surface of 1D MoO_3−x/g-C_3N_4 composite for boosted LED light-driven photoactivity. *J. Mater. Sci.* **2019**, *54*, 5343−5358.
(34) Thangappan, R.; Dhinesh Kumar, R.; Jayavel, R. Facile Synthesis and Characterization of Molybdenum Oxide (MoO_3) Nanofibers and Submicron Rods by Electrospinning Technique for Potential Application in Photocatalytic Activity. *J. Cluster Sci.* **2022**, *33*, 2209−2214.
(35) Li, Y.; Huang, L.; Xu, J.; Xu, H.; Xu, Y.; Xia, J.; Li, H. Visible-light-induced blue MoO_3−C_3N_4 composite with enhanced photocatalytic activity. *Mater. Res. Bull.* **2015**, *70*, 500−505.
(36) Reddy, R. K. K.; Kailasa, S.; Rani, B. G.; Jayarambabu, N.; Yasuhiko, H.; Ramana, G. V.; Rao, K. V. Hydrothermal approached 1-D molybdenum oxide nanostructures for high-performance supercapacitor application. *SN Appl. Sci.* **2019**, *1*, 1365.
(37) Hui, B.; Li, G.; Zhao, X.; Wang, L.; Wu, D.; Li, J.; Via, B. h-MoO_3 microrods grown on wood substrates through a low-temperature hydrothermal route and their optical properties. *J. Mater. Sci.: Mater. Electron.* **2017**, *28*, 3264−3271.
(38) Huang, L.; Xu, H.; Zhang, R.; Cheng, X.; Xia, J.; Xu, Y.; Li, H. Synthesis and characterization of g-C_3N_4/MoO_3 photocatalyst with improved visible-light photoactivity. *Appl. Surf. Sci.* **2013**, *283*, 25−32.
(39) Lee, S. S.; Bai, H.; Liu, Z.; Sun, D. D. Novel-structured electrospun TiO_2/CuO composite nanofibers for high efficient photocatalytic cogeneration of clean water and energy from dye wastewater. *Water Res.* **2013**, *47*, 4059−4073.
(40) Hu, C.; Xu, M.; Zhang, J.; Zhou, Y.; Hu, B.; Yu, G. Recyclable MoO_3 nanobelts for photocatalytic degradation of Rhodamine B by near infrared irradiation. *Int. J. Chem. Kinet.* **2019**, *51*, 3−13.
(41) Vijayan, R.; Joseph, S.; Mathew, B. Green synthesis of silver nanoparticles using Nervalia zeylanica leaf extract and evaluation of their antioxidant, catalytic, and antimicrobial potentials. *Part. Sci. Technol.* **2018**, *37*, 809−819.
(42) Lee, J.; Kim, S. K.; Sohn, Y. Understanding photocatalytic coupled-dye degradation, and photoelectrocatalytic water splitting and CO2 reduction over WO_3/MoO_3 hybrid nanostructures. *J. Ind. Eng.Chem.* **2018**, *62*, 362−374.
(43) Xi, Q.; Liu, J.; Wu, Z.; Bi, H.; Li, Z.; Zhu, K.; Zhuang, J.; Chen, J.; Lu, S.; Huang, Y.; Qian, G. In-situ fabrication of MoO_3 nanobelts decorated with MoO_2 nanoparticles and their enhanced photocatalytic performance. *Appl. Surf. Sci.* **2019**, *480*, 427−437.
(44) Shahzad, H.; Imran, M.; Haider, A.; Naz, S.; Umar, E.; Ul-Hamid, A.; Nabgan, W.; Algaradah, M. M.; Fouda, A. M.; Haider, J.; Ikram, M. Catalytic and antimicrobial properties of Ag and polyacrylic acid doped SrO nanocomposites; molecular docking analysis. *J. Photochem. Photobiol., A* **2023**, *444*, No. 114970.
(45) Desai, N.; Mali, S. Chemically Grown MoO3 Nanorods for Antibacterial Activity Study. *J. Nanomed. Nanotechnol.* **2015**, *6*, 1.
(46) Wang, Y.-W.; Cao, A.; Jiang, Y.; Zhang, X.; Liu, J.-H.; Liu, Y.; Wang, H. Superior Antibacterial Activity of Zinc Oxide/Graphene Oxide Composites Originating from High Zinc Concentration Localized around Bacteria. *ACS Appl. Mater. Interfaces* **2014**, *6*, 2791−2798.
(47) Shinde, V. V.; Dalavi, D. S.; Mali, S. S.; Hong, C. K.; Kim, J. H.; Patil, P. S. Surfactant free microwave assisted synthesis of ZnO microspheres: Study of their antibacterial activity. *Appl. Surf. Sci.* **2014**, *307*, 495−502.
(48) Vijayan, R.; Joseph, S.; Mathew, B. Green synthesis of silver nanoparticles using Nervalia zeylanica leaf extract and evaluation of their antioxidant, catalytic, and antimicrobial potentials. *Part. Sci. Technol.* **2019**, *37*, 809−819.
(49) Zollfrank, C.; Gutbrod, K.; Wechsler, P.; Guggenbichler, J. P. Antimicrobial activity of transition metal acid MoO_3 prevents microbial growth on material surfaces. *Mater. Sci. Eng. C,* **2012**, *32*, 47−54.
(50) Yogananda, H. S.; Nagabhushana, H.; Darshan, G. P.; Basavaraj, R. B.; Daruka Prasad, B.; Sateesh, M. K.; Raghu, G. K. MoO_3 nanostructures from EGCG assisted sonochemical route: Evaluation of its application towards forensic and photocatalysis. *J. Alloys Compd.* **2018**, *745*, 874−891.
(51) Desai, N.; Mali, S.; Kondalkar, V.; Mane, R.; Hong, C.; Bhosale, P. Chemically grown MoO_3 nanorods for antibacterial activity study. *J. Nanomed. Nanotechnol.* **2015**, *6*, 1.

https://doi.org/10.1021/acsomega.3c03910
ACS Omega 2023, 8, 34805−34815

(52) Li, A.; Zhang, M.; Ma, W.; Li, D.; Xu, Y. Sugar-disguised bullets for combating multidrug-resistant bacteria infections based on an oxygen vacancy-engineered glucose-functionalized MoO_3-x photo-coordinated bienzyme. *Chem. Eng. J.* **2022**, *431*, No. 133943.
(53) Weiner, E. R. *Applications of Environmental Chemistry: A Practical Guide for Environmental Professionals*; CRC press, 2010.
(54) Yu, L.; Sun, Y.; Niu, Y.; Zhang, P.; Hu, J.; Chen, Z.; Zhang, G.; Xu, Y. Microenvironment-Adaptive Nanozyme for Accelerating Drug-Resistant Bacteria-Infected Wound Healing. *Adv. Healthcare Mater.* **2023**, *12*, No. 2202596.
(55) Ikram, M.; Chaudhary, K.; Shahzadi, A.; Haider, A.; Shahzadi, I.; Ul-Hamid, A.; Abid, N.; Haider, J.; Nabgan, W.; Butt, A. R. Chitosan/starch-doped MnO_2 nanocomposite served as dye degradation, bacterial activity, and insilico molecular docking study. *Mater. Today Nano* **2022**, *20*, No. 100271.
(56) Shahzadi, I.; Islam, M.; Saeed, H.; Shahzadi, A.; Haider, J.; Haider, A.; Imran, M.; Rathore, H. A.; Ul-Hamid, A.; Nabgan, W.; Ikram, M. Facile synthesis of copolymerized cellulose grafted hydrogel doped calcium oxide nanocomposites with improved antioxidant activity for anti-arthritic and controlled release of doxorubicin for anti-cancer evaluation. *Int. J. Biol. Macromol.* **2023**, *235*, No. 123874.

https://doi.org/10.1021/acsomega.3c03910
ACS Omega 2023, 8, 34805−34815